Artificial magnetic domains by interlayer coupling in an in-plane/perpendicular-to-plane magnetic bilayer system

Klaus M. Seemann [1,2,*] and Florian Kronast [3]

[1] *Université de Lorraine, CNRS, IJL , F-54000 Nancy, France*

[2] *School of Physics and Astronomy, University of Leeds, Leeds LS2 9JT, United Kingdom*

[3] *Helmholtz-Zentrum Berlin für Materialien und Energie, Albert-Einstein-Strasse 15, D-12489 Berlin, Germany*

(Received 17 November 2024; revised 21 March 2025; accepted 12 May 2025; published 23 May 2025)

Artificial magnetic domains are induced into a soft-magnetic in-plane $Co_{60}Fe_{20}B_{19}Si_1$ (CoFeBSi) alloy by interlayer coupling to a perpendicular-to-plane FePt underlayer. We present images documenting the thickness dependence of the size of magnetic domains inside the CoFeBSi ferromagnetic layer. The magnetic domain walls in FePt induce a continuous progression of domain walls into the CoFeBSi at the vicinity of the interface to FePt. With femtosecond laser pulses, the recurrent domain pattern in CoFeBSi has been investigated after reversing the magnetization and we observe a reorganization into the thickness-dependent multidomain state inside the CoFeBSi with strong domain-wall pinning at the interface.

DOI: 10.1103/PhysRevB.111.174439

I. INTRODUCTION

Spintronic devices based on magnetic domain walls for information technology and magnetic sensors rely on current and/or field-driven motion, displacement, or oscillation of domain walls [1]. In materials with high magnetocrystalline anisotropy such as FePt, narrow Bloch-type domain walls with in-plane closure regions capping the Bloch core have been shown to be preferable for the adiabatic and nonadiabatic terms to the spin-transfer torque effect in domain-wall motion experiments [2]. From a point of view of lowering the electrical current densities necessary for rapid domain-wall motion, narrow Nèel-type domain walls in magnetic materials with low magnetocrystalline anisotropy are desirable. The concept of the coupled bilayer magnet [3,4] combines hard and soft magnetic materials to generate novel spin structures and enhance their magnetic properties. In an attempt to artificially create such narrow domain walls via the stray field of narrow Bloch-type walls originating from FePt into a low-anisotropy $Co_{60}Fe_{20}B_{19}Si_1$ of amorphous morphology, we have separated both layers by an insulating Al_xO_y interlayer of 2 nm thickness. CoFeB is a versatile and tunable soft magnetic material in spintronic applications [5–10]. A small amount of 1 atomic percent of the element silicon has been added to replace boron and hence enhance the amorphous morphology of the $Co_{60}Fe_{20}B_{19}Si_1$ compared to $Co_{60}Fe_{20}B_{20}$ by introducing Si as a larger substituent for B. Our findings contribute to understanding the laser-induced magnetic reversal mechanisms of coupled bilayer magnets, which could be interesting for the design of low energy-consumption spintronic or magnonic devices.

*Contact author: k.m.seemann@gmail.com

II. MAGNETOMETRY AND FERROMAGNETIC RESONANCE EXPERIMENTS

The specimen of a magnetically coupled bilayer ($MgO(001)/Fe_{50}Pt_{50}$ [20 nm]/Al_xO_y [2 nm]/$Co_{60}Fe_{20}B_{19}Si_1$ [10 nm]) was grown in two steps. First we deposited the FePt thin film by magnetron-sputter deposition onto a epiready MgO(001) substrate in ultrahigh vacuum. The FePt was grown at 993 K for perpendicular-to-plane ordering [5,11,12]. Subsequently, the specimen was moved to an Argon ion-sputtering system and the Al_xO_y and $Co_{60}Fe_{20}B_{19}Si_1$ were deposited at room temperature onto the FePt in a magnetic field aligned in-plane parallel to the edge of the MgO substrate to induce an anisotropy. An Al_xO_y [1.2 nm] capping layer was deposited to prevent oxidation of the CoFeBSi film and enable imaging by x-ray magnetic circular dichroism photoelectron microscopy (XMCD-PEEM). The bilayer system was characterized magnetically using a MicroSense vibrating-sample magnetometer (VSM) at room temperature in both out-of-plane (marked in blue) and in-plane geometry (red) as illustrated in Fig. 1(a). In out-of-plane geometry the sample specimen is dominated by the FePt underlayer with a coercivity field of 2 kOe, while in in-plane geometry, we obtain a coercitivity field of 8 Oe based on the CoFeBSi top layer. We observe an angle dependence of the magnetic remanence of the CoFeBSi hysteresis in in-plane geometry with a twofold anisotropy, Figure 1(b) originating from a magnetic anisotropy induced during the deposition process and elongated magnetic domains are observed accordingly in the CoFeBSi layer, as illustrated further below.

The coupled bilayer system has been studied by ferromagnetic resonance measurements (FMR) at room temperature using a QuantumDesign NanOsc setup to additionally investigate the spin-wave damping characteristics of the $CoFeBSi/Al_xO_y/FePt$ coupled bilayer magnet system. FMR provide insight into the damping mechanisms in CoFeB-type thin films [13,14]. The FMR measurements were performed in both geometries, in-plane and out-of-plane, varying the

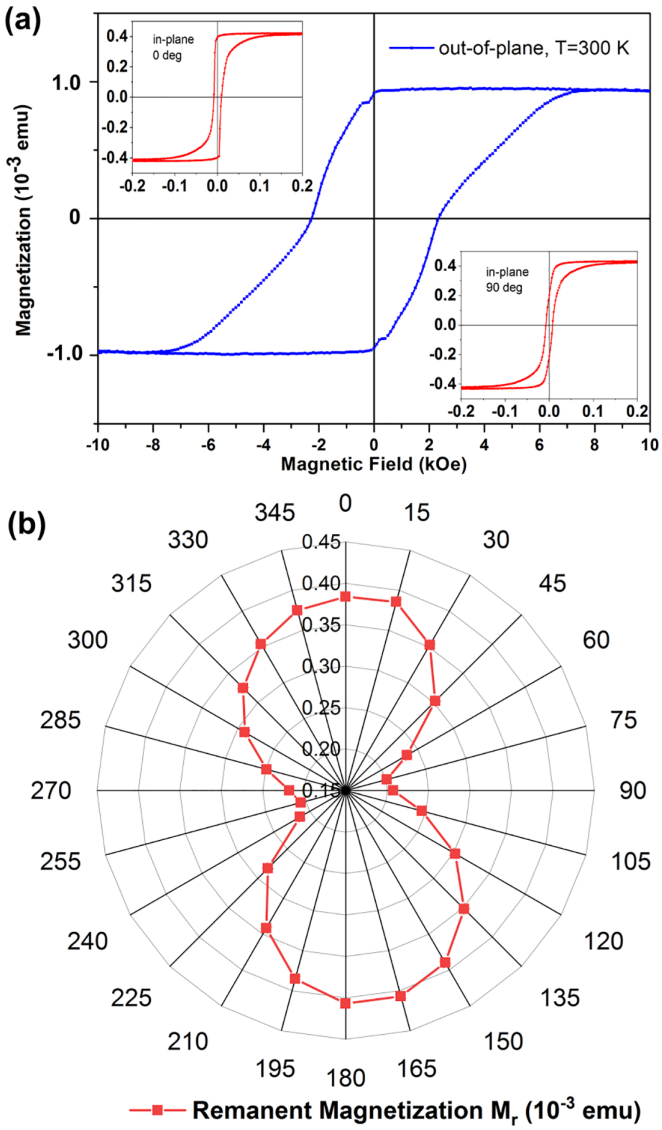

FIG. 1. Hysteretic loops (a) of the CoFeBSi/Al_xO_y/FePt coupled bilayer magnet recorded by vibrating-sample magnetometry at room temperature in out-of-plane (blue) and in-plane geometry (red). In out-of-plane geometry a coercive field of approximately 2 kOe is observed, typical for perpendicularly magnetized ordered FePt, while the in-plane oriented CoFeBSi layer shows a coercive field of 8 Oe. An in-plane anisotropy of the remanent magnetization M_r (at H = 0 Oe) (b) is observed for CoFeBSi showing a maximal M_r at angles 0 and 180°, while a minimum M_r is recorded for the angles 75 and 255°.

magnetic field after first magnetically saturating the system and applying the magnetic field beginning from the state of remanence. The measured derivative of the transmitted power $\frac{dP}{dH}$ through the coupled bilayer magnet is exemplified for some frequencies in Figs. 2(a) and 2(b) for the in-plane and in Figs. 2(e) and 2(f) for the out-of-plane measurement geometry. We display the in-plane $\frac{dP}{dH}$ ranging from 6 GHz to 40 GHz with decreasing magnitude starting from approximately 0.25 kOe of the first resonance to approximately 8 kOe of the eighth resonance. In out-of-plane geometry however, the spin-wave power damping is comparatively weaker in terms of α as compared to the in-plane geometry, with the magnetic field ranging from approximately 19.5 kOe to approximately 26 kOe as obtained from fits to the FMR data, shown in Figs. 2(c) and 2(d) for in-plane and in Figs. 2(g) and 2(h) for out-of-plane geometry. The following formula illustrates the dependence of the FMR on the resonance field H_{res} and the linewidth ΔH, for the actual fitting procedure of the double peaks, a sum of two of these terms has been used to fit the experimental FMR data shown in Figs. 2(a), 2(b), 2(e), and 2(f):

$$\frac{dP}{dH} = k1\frac{4\Delta H(H-H_{res})}{[4(H-H_{res})^2+\Delta H^2]^2} - k2\frac{\Delta H^2-4(H-H_{res})^2}{[4(H-H_{res})^2+\Delta H^2]^2} + c + \delta h, \quad (1)$$

wherein $k1$ and $k2$ are constants, while c takes into account a vertical offset and δh represents a linear background (H × slope) [15].

In the FMR measurements shown in Figs. 2(a) and 2(b), we observe double FMR resonances, i.e., two FMR modes are exhibited experimentally. The damping mode of the FMR signal $\frac{dP}{dH}$ is more pronounced in the in-plane than in the out-of-plane geometry, as shown for linewidth ΔH versus frequency in Figs. 2(c) and 2(g). In the out-of-plane geometry, damping modes 1 and 2 have nearly identical field dependence, whereas damping mode 2 is clearly separated from mode 1 in in-plane geometry. We obtain a similar picture with frequency versus resonant magnetic field split, see Figs. 2(d) and 2(h). Performing a Kittel fit for frequency versus resonance field H_{res} according to

$$f = \frac{\gamma\mu_0}{2\pi}\sqrt{H(H+M_s)}, \quad (2)$$

we find the saturation magnetization M_s and the gyromagnetic ratio $\gamma/2\pi$ [15].

We determine the FMR linewidth broadening ΔH_0 and intrinsic damping α from linewidth ΔH field versus frequency [15] using the following formula

$$\Delta H = \frac{4\pi\alpha}{\gamma}f + \Delta H_0, \quad (3)$$

as summarized in Table I.

It is noteworthy, that the intrinsic damping α of the in-plane mode 1 is approximately twice the value of the out-of-plane mode 1 value. Single-layer CoFeB thin films are reported to show one FMR resonance only. Since the in-plane FMR measurements start at an applied magnetic field of 2.5 kOe in full saturation of the CoFeBSi [see insets of Fig. 1(a)], we attribute the two-mode FMR effect in the in-plane geometry of the coupled bilayer magnet being caused by CoFeBSi (mode 1) on the one hand and FePt (mode 2) on the other hand. In addition to a high intrinsic damping, we also observe a narrowing of the FMR linewidth for the in-plane mode 1, leading according to Eq. (3) to a negative value for ΔH_0, see Table I.

The coupling of the CoFeBSi to the FePt and vice versa causes two in-plane FMR contributions, one from the in-plane rotated FePt spins and one from the in-plane magnetized CoFeBSi. This is supported by the fact that the out-of-plane geometry hysteretic loop of the coupled bilayer system illustrated in Fig. 1(a) has no resemblance to a square hysteretic

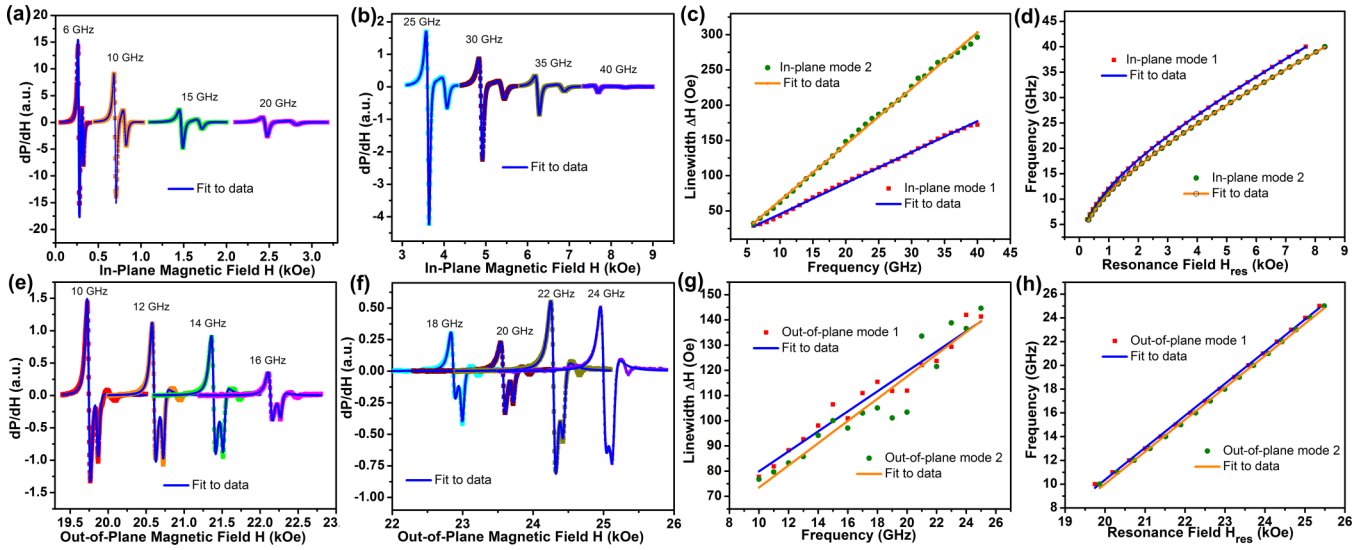

FIG. 2. FMR measurements of the CoFeBSi/Al_xO_y/FePt system performed at 300 K in in-plane geometry at frequencies ranging from 6–40 GHz shown together with fits to the data (a), (b) to determine the resonance field H_{res} and the linewidth ΔH. The experimentally observed resonant damping yields the corresponding in-plane damping parameters inhomogenic linewidth broadening ΔH_0, intrinsic damping α, saturation magnetization $\mu_0 M_s$, and gyromagnetic ratio $\gamma/2\pi$ (c), (d). The resonant magnon damping was also recorded in the out-of-plane geometry for frequencies ranging from 10–24 GHz (e), (f) with associated out-of-plane damping parameters (g), (h).

behavior as expected for a single, out-of-plane magnetized FePt layer, but rather presents itself as a slanted loop. This is caused by the superposition of the in-plane CoFeBSi and the out-of-plane FePt. Therefore, the FMR data exhibits resonance modes, that are hardly separable, see Figs. 2(e)–2(h). Since the out-of-plane measurements are performed at considerably larger magnetic fields above 19.5 kOe, we only observe FMR resonances in the magnetic fully saturated CoFeBSi/Al_xO_y/FePt. It is noteworthy that the FMR out-of-plane modes are closer in terms of damping properties than in the in-plane geometry, see also Table I.

III. MAGNETIC IMAGING BY XMCD-PEEM

To analyze domain formation at the CoFeBSi/FePt interface, we use XMCD-PEEM, a chemically selective and particularly interface-sensitive magnetic imaging technique. Images were taken at the SPEEM instrument of the UE49-PGM microfocus beam line [16,17] of the BESSYII/HZB, which offers tunable x rays with full polarization control, in combination with the possibility to measure in an applied magnetic field [18] or to apply ultrashort laser pulses to quench the magnetic order [19,20]. XMCD arises from a difference in x-ray absorption between right and left circularly polarized light in Fe and Co at the $L_{2,3}$ resonances as a result of the different occupation of the spin-split valence bands [21], providing a strong and chemically selective contrast for imaging magnetic domains. The magnetic sensitivity of the XMCD signal lies along the direction of the incident light, and the XMCD contrast in an image represents a projection of the magnetization onto $\vec{k}$, the wave vector of the incident x-ray beam. In our setup, the angle of incidence of the x-rays was 74°, which makes the instrument more sensitive to in-plane oriented domains. The XMCD contrast I_{XMCD} shown in the images represents the asymmetry value of photoelectron intensities I between two images taken with opposite circular polarizations $\sigma+$ and $\sigma-$, i.e.,

$$I_{XMCD} = \frac{I_{\sigma+} - I_{\sigma-}}{I_{\sigma+} + I_{\sigma-}}. \quad (4)$$

The images were recorded using secondary electrons with an escape depth (or information depth) of around 3–5 nm. For this purpose, the top layer had to be thinned by Ar ion milling to make the interface accessible for PEEM. The Argon ion milling has been carried out until revealing the interface of the CoFeBSi to the FePt underlayer. Hence, a pinhole

TABLE I. Damping parameters inhomogenic linewidth broadening ΔH_0, intrinsic damping α, saturation magnetization $\mu_0 M_s$, and gyromagnetic ratio $\gamma/2\pi$ obtained from in-plane and out-of-plane ferromagnetic resonance measurements of the CoFeBSi/Al_xO_y/FePt coupled bilayer system measured at 300 K and in full magnetic saturation.

	ΔH_0 (Oe)	α	$\mu_0 M_s$ (T)	$\gamma/2\pi$ (GHz/T)
In-plane mode 1	-15.0 ± 0.5	0.011 ± 0.001	1.68 ± 0.05	29.26 ± 0.30
In-plane mode 2	1.5 ± 0.1	0.006 ± 0.001	1.42 ± 0.01	29.26 ± 0.29
Out-of-plane mode 1	40.2 ± 1.0	0.005 ± 0.001	1.61 ± 0.01	26.99 ± 0.01
Out-of-plane mode 2	29.4 ± 1.0	0.006 ± 0.001	1.63 ± 0.01	26.96 ± 0.01

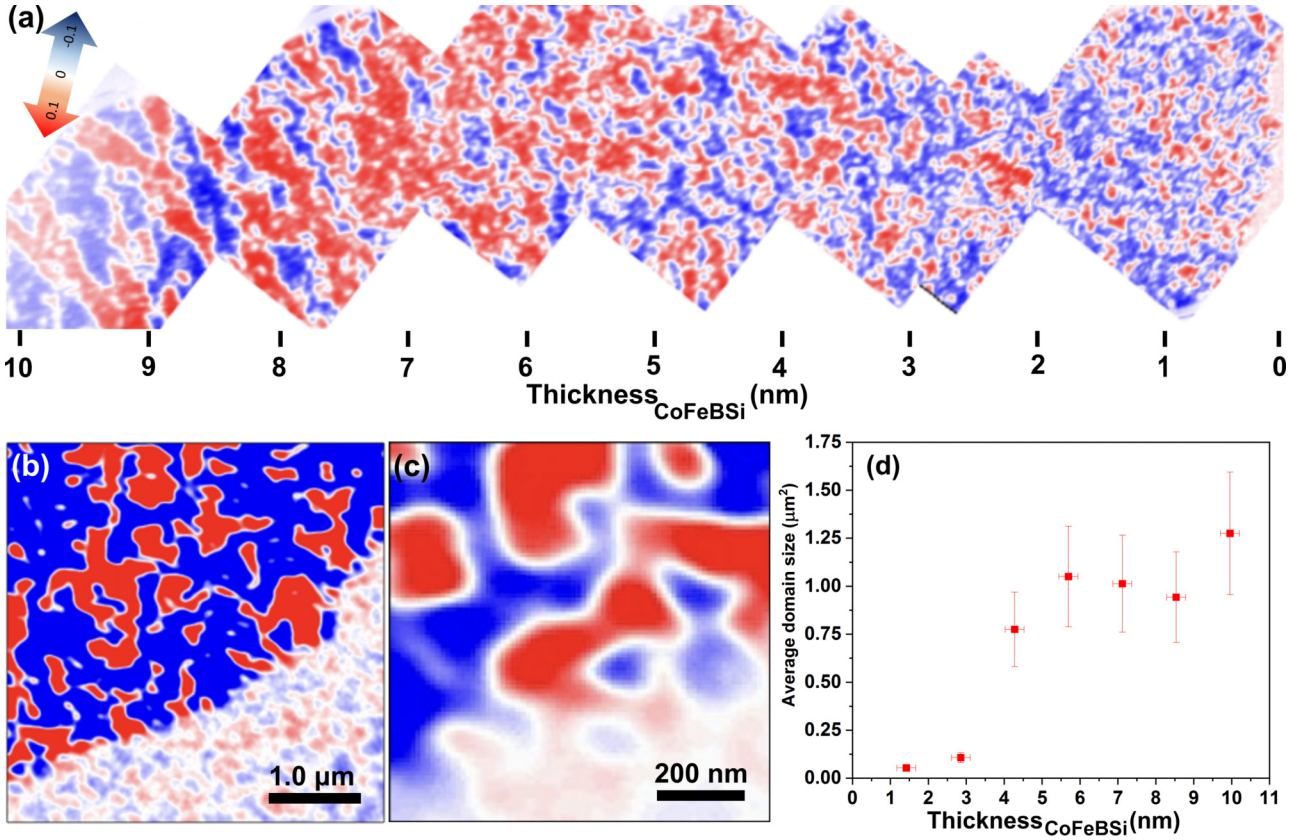

FIG. 3. Top view of a puzzle fit (a) of seven XMCD-PEEM 3-µm field of views along a wedge of CoFeBSi starting at the FePt interface (right) to a thickness of 10 nm (left) showing the evolution of the artificial magnetic domains induced by the FePt underlayer. The color coding of the magnetization along the direction of beam incidence is indicated by the arrow top left. The interface of CoFeBSi and FePt is separated by 2 nm of aluminum oxide layer. The induced magnetic domains are illustrated as top views at various XMCD-PEEM magnifications recorded at the Fe-L_3 edge of 707 eV (b), (c). The notably weaker contrast in the lower right corner of the images originates from the out-of-plane magnetized FePt in comparison to the much stronger contrast of the in-plane magnetized CoFeBSi. (d) Average domain size in the CoFeBSi as a function of the thickness.

structure has been prepared *in situ* by Argon ion milling through an aperture located above the sample and as a consequence, microscopically a thin-film wedge at the edge of the pinhole structure has been created in the CoFeBSi.

In Fig. 3(a) the magnetic domain pattern of a wedge starting at the interface through to the overall thickness of 10 nm of the CoFeBSi layer were obtained by XMCD-PEEM at room temperature in zero field after demagnetization. In total, seven images were fit together to depict the thickness-dependent magnetic domain structure along the CoFeBSi wedge. CoFeBSi shows small magnetic domains induced by the FePt underneath via stray-field coupling of the FePt magnetic domains and field closure in the CoFeBSi in-plane-oriented magnetic domains. We attribute this to a reorientation of the local magnetic spins of domains and the associated walls. The analysis of the topology of noncollinear spins in transition from FePt to CoFeBSi lies beyond the frame of this work. The domain walls continuously propagate into the CoFeBSi and the domain size is similar to FePt, i.e., of the labyrinth type as visible in Fig. 3(c). The Néel capping of the Bloch-type magnetic domain wall in FePt transgresses into a Néel-type magnetic domain wall within the CoFeBSi, continuously maintaining the wall width at the interface and spreads out into the regions of increased thickness of the CoFeBSi thereafter. The CoFeBSi top layer exhibits an anisotropic domain structure in the thickness regime from 8 nm to 10 nm [see also Fig. 3(a) left side]. We have analyzed the evolution of the domain size in the CoFeBSi as a function of thickness as shown in Fig. 3(d). From a CoFeBSi thickness of approximately 3 nm for which we determine an average domain size of ≈0.1 µm^2, the average magnetic domain size increases considerably by an order of magnitude to ≈1.0 µm^2 from a CoFeBSi thickness of 6 nm and stagnates at this average domain size to CoFeBSi thickness of 9 nm, the maximum average domain area being reached at 10 nm CoFeBSi with ≈1.25 µm^2.

Even though we observe a magnetic domain evolution in the CoFeBSi that is caused by a strong coupling to the FePt through the Al_xO_y interlayer to a CoFeBSi thickness of 3 nm followed by a weakly coupling CoFeBSi from a thickness of approximately 4–5 nm onwards [see Fig. 3(d)], the magnetic domains are erased in the magnetic field applied for the in-plane FMR measurements as described above. Hence, the discontinuity in the average domain-size pattern visible in the XMCD-PEEM images of Fig. 3(a) and even more obvious in Fig. 3(d) cannot account for two FMR modes in the in-plane measurement geometry. The anisotropy in directionally elongated magnetic domains observable from a CoFeBSi

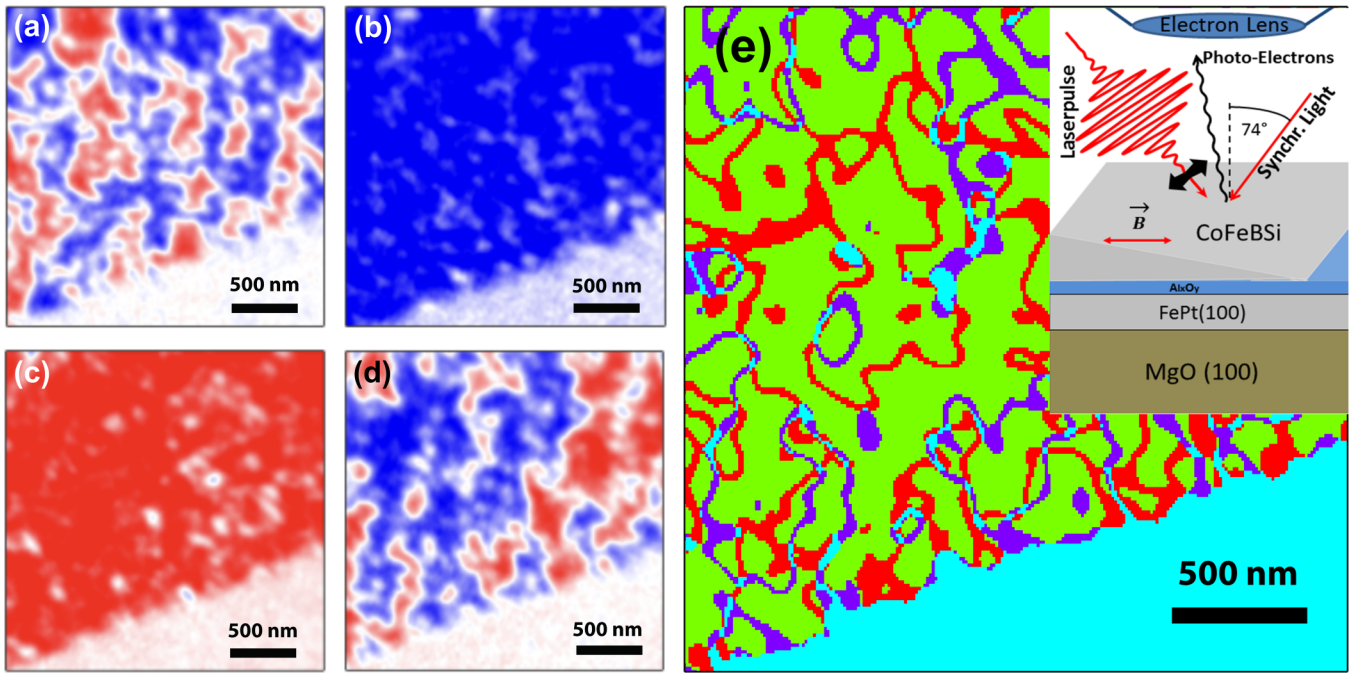

FIG. 4. Top views of consecutive laser-induced reversal of the magnetic domains in CoFeBSi from the demagnetized state (a) assisted by an external in-plane-oriented magnetic field of +150 Oe (b) and −150 Oe (c). The laser pulse reverses the magnetization of the CoFeBSi and the free FePt (low-intensity area of the image). The images show the wedge-shaped transition to a thickness of 2 nm of CoFeBSi (high-intensity area of the image). (d) Final field-free recurrence of the CoFeBSi into a multidomain state. (e) Lateral displacement of the induced domain walls in CoFeBSi before and after applying a femtosecond laser pulse in zero applied field. The magnetic domains of uniform magnetization (green) are separated by narrow Nèel-type walls. The initial state of the induced domain walls are shown in red, while the final state of domain walls after applying a laser pulse is displayed in magenta. The bright blue color code corresponds to matching domain-wall positions. A cross-sectional schematic of the wedge structure including the measurement geometry (not to scale) is depicted in the inset of the right upper corner.

thickness of 7 nm onwards to the total film thickness of 10 nm [see Fig. 3(d)] is possibly a signature of the twofold anisotropy in remanence of CoFeBSi seen in Fig. 1(b). However, this also cannot cause the emergence of two FMR modes observed in in-plane geometry, as the CoFeBSi film was completely saturated.

The interface between FePt, Al_xO_y, and the CoFeBSi was investigated at both the Fe-L_3 and Co-L_3 edges to confirm the domain pattern of FePt, which is only visible in the images based on Fe-L_3-XMCD, but not in the Co-L_3-XMCD images. Hence, only Fe_3-based images are shown in Figs. 3(a)–3(c). The domain-size analysis based on the CoFeBSi wedge allows for choosing a suitable thickness value to yield a desired domain structure, when induced from an FePt underlayer as described. We identify this thickness regime from our results shown in Fig. 3 ranging up to a thickness of approximately 3 nm of CoFeBSi. From a thickness of 4 nm the average magnetic domain size increases dramatically. We did not observe a region of perpendicularly magnetized CoFeBSi at the interface to the FePt separated by a 2-nm thick Al_xO_y spacer layer.

IV. INTERFACIAL ANALYSIS BY ULTRAFAST MAGNETIZATION REVERSAL

Complementary, we study the interfacial response to ultrafast laser pulses [22,23], see also schematic in the inset to Fig. 4(e). Figure 4(a) illustrates the CoFeBSi/Al_xO_y/FePt interface region in the demagnetized state, the CoFeBSi represents here a thickness of 0.5 nm at the top left corner, decreasing continuously, reaching the FePt underlayer at the lower right part of the image.

We observed that using a magnetic field in in-plane orientation with a field strength of 150 Oe did not suffice to reverse or annihilate the magnetic domains in CoFeBSi at the very interface to Al_xO_y/FePt due to a much stronger coupling of CoFeBSi to FePt at a CoFeBSi thicknesses below 2 nm, contrary to a CoFeBSi thickness of 10 nm in the same sample, as observed in the hysteretic loops of Fig. 1(a). It is known that a decreasing CoFeB thickness below 2 nm can lead to an increasing anisotropy at interfaces [8]. Similarly, we observe an enhancement of coupling of CoFeB within the CoFeBSi/Al_xO_y/FePt at a CoFeBSi thickness below 2 nm.

Hence, to reconfigure the domain state along the CoFeBSi/Al_xO_y/FePt interface we use femtosecond laser pulses in combination with a small magnetic bias field in in-plane direction. The utilized titanium sapphire laser has a fundamental wavelength of 800 nm and pulse duration of 100 fs. The laser has an incidence angle of 74° to the sample surface and a spot size of approximately 15 × 50 μm^2. The magnetic switching experiments were performed using single pulses with a laser fluence of 12 $mJcm^{-2}$.

We applied an in-plane magnetic field of +150 Oe, sent a laser pulse to the CoFeBSi/Al_xO_y/FePt interface, and

imaged by XMCD-PEEM as shown in Fig. 4(b). The laser pulse demagnetizes the CoFeBSi and upon remagnetization in the applied field, the magnetic domains were erased to form one uniform direction of magnetization. Likewise, we subsequently applied a magnetic field in the opposite direction of −150 Oe and again applied a laser pulse at the same region. Accordingly, we obtained a uniformly magnetized region in the opposite direction upon remagnetization in the applied field, illustrated in Fig. 4(c). This procedure guarantees a pristine coupling mechanism to act on the fully saturated CoFeBSi from the perpendicular-to-plane magnetic FePt upon a laser pulse reinstating the multidomain state in the CoFeBSi in zero applied field. The images in Figs. 4(b) and 4(c) were recorded in zero-field condition, i.e., the magnetic field was applied only prior and during the laser pulse. The magnetic field strength of 150 Oe applied in in-plane geometry is not sufficient to change the magnetic domain state of the CoFeBSi without laser pulsing. The CoFeBSi recurs back to a multidomain state upon applying a laser pulse in zero field, as shown in Fig. 4(d). Comparing the initial and final multidomain state Figs. 4(a) and 4(d), we notice that both initial and final domain structure are not exactly identical. We attribute this to a reconfiguration of the FePt interface after applying femtosecond laser pulses in conjunction with a magnetic field in combination with reverse coupling from the CoFeBSi magnetically saturated in-plane. The FePt is visibly affected by the field-assisted laser switching as can be seen from the change in magnetic XMCD contrast in the lower right corner of Figs. 4(a)–4(c). Hence, after laser pulsing in the presence of a magnetic field of 150 Oe in in-plane direction, we also observe a saturation within the FePt. A transient reorganization of magnetic anisotropy causing a temporary in-plane canting of magnetization in CoPd films was observed previously at lower Oersted field and laser fluence [19].

Additionally, we analyze the change in magnetic domain state of initial [Fig. 4(a)] and recurrent magnetic domain pattern [Fig. 4(d)] of the CoFeBSi wedge structure by overlaying and color coding the difference map to illustrate the regions where domain walls are mobile and regions governed by domain-wall pinning. The result is displayed in Fig. 4(e). The lateral displacement of the induced magnetic domain walls in CoFeBSi before and after applying a femtosecond laser pulse in zero applied field is more pronounced for increasing CoFeBSi thickness [upper left part of Fig. 4(e)] as compared to the region at the vicinity of the interface. The magnetic domains of uniform magnetization (green) are separated by narrow Nèel-type walls. The initial state of the induced domain walls are shown in red, while the final state of domain walls after applying a laser pulse is displayed in magenta. The bright blue color code corresponds to matching domain-wall positions. This pinning effect appears to be strongest directly at the interfacial border between both magnets at the proximity of in-plane magnetization of the CoFeBSi and the out-of-plane oriented FePt.

In summary, we investigated the generation of artificial magnetic domain walls in a CoFeBSi/Al_xO_y/FePt coupled bilayer magnet and observed an interesting artificial system of magnetic domain walls in the CoFeBSi. We found two pronounced FMR modes in in-plane geometry, one mode with a large Gilbert damping constant originating from CoFeBSi and one mode with a Gilbert damping constant of approximately half of the first mode due to FePt. Using high-resolution XMCD-PEEM we elucidated the continuous transgression of the Néel capping of the Bloch-type magnetic domain walls in FePt, generating actual Néel-type magnetic domain walls in the in-plane CoFeBSi layer suggesting a similar width of the magnetic domain walls at the interface of the CoFeBSi/FePt. The domain-wall width inside the CoFeBSi is obviously induced by the Néel capping of FePt Bloch-type domain wall. The size of the artificially created magnetic domains inside CoFeBSi has a strong dependence on the thickness of the CoFeBSi due to increasing dipolar coupling within the CoFeBSi with increasing film thickness and vertical distance from the interface to the perpendicular-to-plane FePt. While more experimental evidence will be needed involving a range of different materials, our data so far suggests that a much narrower magnetic domain-wall width may be induced in ultrathin layers of materials with low magnetocrystalline anisotropy such as CoFeBSi by coupling to a magnetic material with high magnetocrystalline anistotropy such as FePt. This could make such multilayer systems interesting for increased efficiency in spin-torque transfer devices, for example. In additional femtosecond laser-pulse switching we studied the domain pattern after remagnetization and detect a strong domain-wall pinning effect at the interface between FePt and CoFeBSi. Assisted by a magnetic field we are able to reverse the magnetization with a laser pulse inside the CoFeBSi along the magnetic-field direction. Subsequently, in zero applied magnetic field, we observe a reorganization into a thickness-dependent multidomain state inside the CoFeBSi, which however is not exactly identical to the domain pattern of the initial state.

ACKNOWLEDGMENTS

K.M.S. gratefully acknowledges funding by the SONOMA Project cofunded by FEDER-FSE Lorraine et Massif des Vosges 2014-2022, a European Union Program. We also thank C. Rojas-Sanchez for assistance, C. H. Marrows for help with the sample preparation, and S. Mangin for critically reviewing the manuscript. We thank the Helmholtz-Zentrum Berlin für Materialien und Energie for the allocation of synchrotron radiation beam time.

[1] E. Y. Vedmedenko, R. K. Kawakami, D. D. Sheka, P. Gambardella, A. Kirilyuk, A. Hirohata, C. Binek, O. Chubykalo-Fesenko, S. Sanvito, B. J. Kirby, J. Grollier, K. Everschor-Sitte, T. Kampfrath, C.-Y. You, and A. Berger, The 2020 magnetism roadmap, J. Phys. D: Appl. Phys. **53**, 453001 (2020).

[2] C. H. Marrows, Spin-polarised currents and magnetic domain walls, Adv. Phys. **54(8)**, 585 (2005).

[3] E. E. Fullerton, J. S. Jiang, M. Grimsditch, C. H. Sowers, and S. D. Bader, Exchange-spring behavior in epitaxial hard/soft magnetic bilayers, Phys. Rev. B **58**, 12193 (1998).

[4] E. F. Kneller and R. Hawig, The exchange-spring magnet: a new material principle for permanent magnets, IEEE Trans. Magn. **27**, 3588 (1991).

[5] K. M. Seemann, F. Freimuth, H. Zhang, S. Blügel, Y. Mokrousov, D. E. Bürgler, and C. M. Schneider, Origin of the planar Hall effect in nanocrystalline $Co_{60}Fe_{20}B_{20}$, Phys. Rev. Lett. **107**, 086603 (2011).

[6] M. Arif, X. Zhang, M. Amir, E. Lui, and F. Xu, Tailoring the magnetism and spin dynamics in CoFeB thin films by post annealing for spintronics applications, J Mater Sci: Mater Electron **34**, 574 (2023).

[7] Y. Huang, R. Chen, and Z. Xu, Investigation of magnetic properties in thick CoFeB alloy films for controllable anisotropy, Appl. Phys. A **122**, 98 (2016).

[8] P. G. Gowtham, G. M. Stiehl, D. C. Ralph, and R. A. Buhrman, Thickness-dependent magnetoelasticity and its effects on perpendicular magnetic anisotropy in Ta/CoFeB/MgO thin films, Phys. Rev. B **93**, 024404 (2016).

[9] D. D. Lam, F. Bonell, Y. Shiota, S. Miwa, T. Nozaki, E. Tamura, N. Mizuochi, T. Shinjo, Y. Suzuki, and S. Yuasa, Growth of perpendicularly magnetized thin films on a polymer buffer and voltage-induced change of magnetic anisotropy at the MgO|CoFeB interface, AIP Adv. **5**, 067132 (2015).

[10] L. Baldrati, A. J. Tan, M. Mann, R. Bertacco, and G. S. D. Beach, Magneto-ionic effect in CoFeB thin films with in-plane and perpendicular-to-plane magnetic anisotropy, Appl. Phys. Lett. **110**, 012404 (2017).

[11] K. M. Seemann, Y. Mokrousov, A. Aziz, J. Miguel, F. Kronast, W. Kuch, M. G. Blamire, A. T. Hindmarch, B. J. Hickey, J. Miguel, I. Souza, and C. H. Marrows, Spin-orbit strength driven crossover between intrinsic and extrinsic mechanisms of the anomalous Hall effect in the epitaxial $L1_0$-ordered ferromagnets FePd and FePt, Phys. Rev. Lett. **104**, 076402 (2010).

[12] K. M. Seemann, F. Garcia-Sanchez, F. Kronast, J. Miguel, A. Kákay, C. M. Schneider, R. Hertel, F. Freimuth, Y. Mokrousov, and S. Blügel, Disentangling the physical contributions to the electrical resistance in magnetic domain walls: A multiscale study, Phys. Rev. Lett. **108**, 077201 (2012).

[13] X. Liu, M. J. Carter, and G. Xiao, Ferromagnetic resonance and damping properties of CoFeB thin films as free layers in MgO-based magnetic tunnel junctions, J. Appl. Phys. **110**, 033910 (2011).

[14] C. Lacroix, K. Oguz, J. M. D. Coey, and D. Ménard, Ferromagnetic resonance damping mechanisms in CoFeB thin films with Cr substitution, Phys. Rev. B **108**, 094402 (2023).

[15] G. Woltersdorf, Spin-pumping and two-magnon scattering in magnetic multilayers, Ph.D. thesis, Simon Fraser University, 2004.

[16] F. Kronast, J. Schlichting, F. Radu, Sh. Mishra, T. Noll, and H. A. Dürr, Spin-resolved photoemission microscopy and magnetic imaging in applied magnetic fields, Surf. Interface Analysis **42**, 1532 (2010).

[17] F. Kronast and S. Molina, SPEEM: The photoemission microscope at the dedicated microfocus PGM beamline UE_{49}-PGMa at BESSY II, Journal of large-scale research facilities (JLSRF) **2**, A90 (2016).

[18] O. Sandig, J. Herrero-Albillos, F. M. Römer, N. Friedenberger, J. Kurde, T. Noll, M. Farle, and F. Kronast, Imaging magnetic responses of nanomagnets by XPEEM, J. Electron Spectrosc. Relat. Phenom. **185**, 365 (2012).

[19] V. López-Flores, M. A. Mawass, J. Herrero-Albillos, A. A. Ünal, S. Valencia, F. Kronast, and C. Boeglin, A local view of the laser induced magnetic domain dynamics in CoPd stripe domains at the picosecond time scale, J. Phys.: Condens. Matter **32**, 465801 (2020).

[20] A. Arora, M. A. Mawass, O. Sandig, C. Luo, A. A. Ünal, F. Radu, S. Valencia, and F. Kronast, Spatially resolved investigation of all optical magnetization switching in TbFe alloys, Sci. Rep. **7**, 9456 (2017).

[21] G. Van der Laan, Sum rules and beyond, J. Electron Spectrosc. Relat. Phenom. **101–103**, 859 (1999).

[22] A. Kirilyuk, A. V. Kimel, and T. Rasing, Laser-induced magnetization dynamics and reversal in ferrimagnetic alloys, Rep. Prog. Phys. **76**, 026501 (2013).

[23] G. Kichin, M. Hehn, J. Gorchon, G. Malinowski, J. Hohlfeld, and S. Mangin, From multiple- to single-pulse all-optical helicity-dependent switching in ferromagnetic Co/Pt multilayers, Phys. Rev. Appl. **12**, 024019 (2019).